Journal of The Electrochemical Society





# Albumin Protein Adsorption on CoCrMo Implant Alloy: Impact on the Corrosion Behaviour at Localized Scale

*Journal of The Electrochemical Society*, 2022 **169** 031507

# Albumin Protein Adsorption on CoCrMo Implant Alloy: Impact on the Corrosion Behaviour at Localized Scale

**Ehsan Rahimi,[1] Ruben Offoiach,[1] Kitty Baert,[2] Herman Terryn,[2] Lorenzo Fedrizzi,[1] and Maria Lekka[3,z]**

[1]*Department of Engineering and Architecture, University of Udine, 33100 Udine, Italy*
[2]*Vrije Universiteit Brussel, Department of Materials and Chemistry, Research Group Electrochemical and Surface Engineering, 1050 Brussels, Belgium*
[3]*CIDETEC, Basque Research and Technology Alliance (BRTA), 20014 DonostiaSan Sebastián, Spain*

The protein adsorption and both its conformational arrangements and electrochemical interactions on the surface of metallic biomaterials has an immense impact on corrosion/biodegradation and biocompatibility of implantable metals. In this study, we used scanning Kelvin probe force microscopy (SKPFM) to reveal the synergistic effect of various bovine serum albumin (BSA) concentrations and overpotential conditions on BSA protein adsorption mechanisms and its influence on the corrosion behaviour of the CoCrMo alloy in phosphate-buffered saline solution. Electrochemical measurements showed that CoCrMo alloy was more resistant to corrosion in the 2 g $l^{-1}$ BSA protein medium than in the 0.5 g $l^{-1}$ one. The SKPFM analysis revealed a lower surface potential on the regions where BSA was adsorbed forming clusters, than on the un-covered CoCrMo substrate. When the surface overpotential and the protein concentration were increased from the OCP to +300 mV vs Ag/AgCl and from 0.5 to 2 g $l^{-1}$, respectively, on both protein covering and surface potential were increased. Field emission scanning electron microscopy indicated that localized corrosion eventually occurred at the BSA protein/substrate interface owing to the adsorption of counterions and the difference between the surface potential values.

 [DOI: 10.1149/1945-7111/ac5a1b]

Manuscript submitted November 3, 2021; revised manuscript received February 13, 2022. Published March 14, 2022. *This paper is part of the JES Focus Issue on Women in Electrochemistry.*

Nowadays, metals and alloys play an outstanding role in the biomedical field and are mainly used as implant materials in orthopaedic, dental, cardiovascular, and fracture-fixing components.[1,2] To determine suitable implant materials for a specific application, different properties such as mechanical and corrosion resistances, biocompatibility, and toxicity must be considered.[3,4] However, the physiological media of the human body constitute a complex corrosive environment consisting of various ions, proteins, and cells in which different alloys such as the most used Ti6Al4V, CoCrMo, or stainless steels are susceptible to degradation and corrosion following different mechanisms.[5–7] When an implant is exposed to the environment in a human body, protein is initially adsorbed, which in turn plays a predominant and determinative role in subsequent interactions.[8,9]

Tissue compatibility and cell adhesion are both controlled by the initial interaction between serum proteins and the implant.[2] The conformation and amount of the protein layer adsorbed on the implant are both influenced by surface properties such as the surface energy, topography, hydrophobicity, and chemical composition of the metal oxide layer on the implant.[10] For example, Guerra et al.[11] demonstrated that by adding methyl groups to a vinyl polymer side chain, the conformation and distribution of the fibronectin protein adsorbed on an implant changed from globular to network morphology owing to changes in the implant surface chemistry. In contrast, the protein adsorption mechanism can be influenced by the ionic strength, agitation, and pH of the solution and the size, charge, and concentration of the protein molecule.[10,12]

To date, biocompatible cobalt-based alloys (particularly CoCrMo) have been extensively used in surgical implants such as hip and knee joint replacements because of their overall high corrosion resistance and perfect wear properties.[13,14] The spontaneous compact oxide layer formation on the surface of implant alloys such as CoCrMo, which is mainly composed of $Cr_2O_3$, considerably inhibits the release of metal ions during contact with human physiological fluids and tissues.[14,15] However, the dynamic conditions of the human body trigger the mechanical abrasion of the oxide film on metallic implant materials and then accelerate corrosion with the release of metal ions and oxide complexes in vivo.[1] Complex oxide films exhibiting *n*- or *p*-type semiconductor characteristics and other atomic defects are susceptible to localized degradation such as pitting or crevice attacks due to interactions with aggressive ions such as $Cl^-$, protein adsorption, or protein–metal complex detachment.[6,16,17]

The atomic bonding of proteins to various metal atoms in implant oxide layers strongly depends on the surface chemistry of the oxide layer including the chemical composition, crystallinity, and defect density.[2,10] Different groups have studied the adsorption mechanisms of protein molecules on solid surfaces as well as the electrochemical interactions between protein molecules and implant surfaces and the corresponding corrosion mechanisms by infrared and Raman spectroscopies,[18,19] ellipsometry,[20,21] quartz crystal microbalance,[22–24] atomic force microscopy (AFM),[25–29] scanning tunnelling microscopy (STEM),[30,31] transmission electron microscopy (TEM),[32,33] X-ray photoelectron spectroscopy (XPS),[34–36] simulation studies,[37,38] electrochemical measurements,[4,5,15,16,39] and scanning Kelvin probe force microscopy (SKPFM).[12,26]

The concept of measuring the difference between the work function energies (WFEs) of two materials was initially established by Lord Kelvin[40] and was physically extended to a Kelvin or capacitive probe and then improved by some researchers.[41,42] Higher-WFE materials are nobler than lower-WFE ones or are less active in electrochemical interactions.[43,44] Therefore, metals exhibiting a low surface Volta potential (which is directly correlated with WFE) also exhibit high electrochemical activity, which, in turn, is a useful parameter for predicting the degradation mechanism.[45,46] For biological molecules such as DNA and proteins, SKPFM can be used to analyse the native property of a bound molecule owing to the molecular surface charge.[47,48] Therefore, the local electrical surface potential analysis represents a correlation between a heterogeneous bimolecular layer (i.e. a monolayer or multilayer) and the molecular-level structure[49] For example, Leung et al.[50] indicated that the lower surface potential of a DNA molecule with respect to the matrix was related to the molecular nanostructure because DNA molecules consist of a negatively charged phosphate backbone, which leads to a highly negative charge on the DNA surface.

Nevertheless, the correlation between the surface potential of the adsorbed protein and the surface potential (direct relationship with

[z]E-mail: mlekka@cidetec.es

work function energy) of the oxide layer on metallic implants and their role in micro-/nano-degradation remains unclear. Therefore, in this research, the conformational and morphological changes of bovine serum albumin (BSA) were systematically characterised during protein adsorption on a CoCrMo oxide layer under different overpotential conditions including an open-circuit potential (OCP), +100 mV, and +300 mV vs Ag/AgCl in phosphate-buffered saline (PBS) solution. A multi-technique procedure was used, including electrochemical measurements, AFM/SKPFM, XPS, and field-emission scanning electron microscopy (FE-SEM) to reveal the BSA protein conformational arrangement and its surface potential distribution at the corrosion initiation sites on the CoCrMo alloy surface.

## Experimental

***Materials and preparation.***—The ASTM F1537 low-carbon CoCrMo alloy was used in this study. The chemical composition (wt%) of the alloy was 0.05 C, 0.39 Si, 0.45 Mn, 0.004 P, 0.001 P, 27.77 Cr, 5.08 Mo, 0.25 Ni, 65.6 Co, 0.005 Ti, 0.38 Fe, and 0.22 N. Specimens (5-$cm^2$ surface area) were used for electrochemical measurements, and other specimens (0.8-$cm^2$ surface area) were used for microstructural characterisation and AFM/SKPFM measurements. The samples were mechanically ground and polished to a mirror-like surface, washed with ethanol, ultrasonicated in acetone for 30 min, and finally blow-dried with air prior to characterisation. All the samples used for the surface analysis and microscopic measurements were stored in a desiccator at room temperature.

***Electrolyte and electrochemical measurements.***—The electrochemical measurements of the CoCrMo alloy were performed in PBS solution containing 8 g $l^{-1}$ of NaCl, 0.2 g $l^{-1}$ of KCl, 1.15 g $l^{-1}$ of $Na_2HPO_4$, and 0.2 g $l^{-1}$ of $KH_2PO_4$ following the ASTM Standard (F2129).[51] To investigate the BSA protein adsorption and interaction with the metal substrate, different concentrations (i.e. 0, 0.5, 1, or 2 g $l^{-1}$) of BSA (lyophilised powder; Sigma–Aldrich; ⩾96% agarose gel electrophoresis) were added to the PBS solution. Electrochemical measurements were carried out using an Avesta cell according to the method developed by Qvarfort[52] and a conventional three-electrode electrochemical cell. This method was used to eliminate crevice corrosion around the specimen holder, thereby allowing temperature control. The electrolyte pH was adjusted using a pH meter (GLP 21, CRISON) approximately in the range 7.4 ± 0.1, and the temperature was maintained at 37 °C for all the measurements. An AUTOLAB PGSTAT30 potentiostat instrument plus an $Ag/AgCl/KCl_{3\ M}$ electrode [+222 mV vs standard hydrogen electrode (SHE)] and a platinum wire were used as the reference and counter electrodes, respectively. All the electrochemical measurements were recorded after the specimens had been immersed in the solution for 1 h to stabilise the OCP. Potentiodynamic polarization (PDP) measurements were scanned at 1 $mV.s^{-1}$ from the cathodic to the anodic potentials. Electrochemical impedance spectroscopy (EIS) measurements were performed after the specimens had been immersed in PBS solution containing various protein concentrations for 1 h and different overpotential conditions (at OCP, +100 mV, or +300 mV vs Ag/AgCl) in the range 10 mHz to 10 kHz by applying a ±10 mV sinusoidal excitation signal.

***Microstructural characterisation and AFM/SKPFM measurements.***—The BSA protein adsorption on the complex oxide layer of the CoCrMo alloy was examined using AFM, SKPFM, and FE-SEM. All the measurements were performed on polished specimens ultrasonically cleaned in acetone for 20 min without any electrochemical etching. The microstructures of the CoCrMo surfaces exposed to the PBS solution containing 0.5 or 2 g $l^{-1}$ of BSA were examined using an FE-SEM (JEOL, JSM-7610FPlus) instrument equipped with an Oxford Instruments X-MAX20 energy-dispersive X-ray spectroscopy (EDXS) probe at a working distance of 15 mm and operating at an acceleration voltage of 5 kV and in secondary electron (SE) mode. AFM/SKPFM maps were utilized to evaluate the topography and surface potential of the BSA protein adsorbed on the CoCrMo surface under different overpotential conditions (i.e. OCP, +100 mV, and +300 mV vs Ag/AgCl). The AFM/SKPFM device was a Digital Instruments Nanoscope IIIa Multimode equipped with a pyramidal *n*-type doped silicon PtIr5-coated single-crystal tip (SCM-Pit probe). Surface potential maps were obtained using the dual-scan mode. In the first scan, topography data was obtained using the tapping mode, and the second scan surface potential was captured by lifting the tip to 100 nm above the specimen surface. Topography and surface potential maps were captured in air at 27 °C at a relative humidity of approximately 28% using a pixel resolution of 512 × 512, a zero-bias voltage, and a scan frequency of 0.2 Hz. The histogram and power-spectral-density (PSD) analyses based on multimodal Gaussian distributions (MGDs) and fast Fourier transform (FFT), respectively, were used to more precisely interpret the surface potential on the complex and heterogeneous surfaces affected by the various BSA protein shapes and morphologies according to the procedure followed in previous studies.[46,53]

***X-ray photoelectron spectroscopy (XPS).***—The chemical composition of the CoCrMo surface layer was analysed using a PHI-5000 Versaprobe-II (Physical Electronics) equipped with a monochromatic Al Kα X-ray source (operating at 1486.71 eV) at a spot diameter of 100 $\mu$m to measure surface compositions up to *ca.* 10 nm deep. The irradiation power of the X-ray beam was 25 W. The

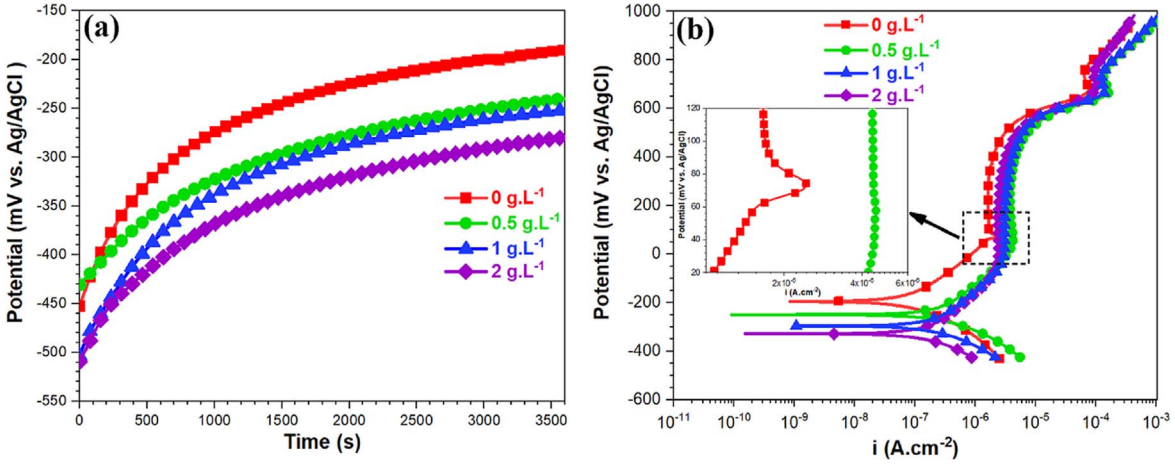


**Figure 1.** (a) OCP and (b) the potentiodynamic polarization measurements of CoCrMo alloy in PBS solution with various concentrations of BSA protein at 37 °C, pH 7.4, and aerated conditions.

kinetic energy of the photoelectrons was measured at a 45° take-off. The vacuum in the analysis chamber was approximately $1 \times 10^{-9}$ torr. The XPS results were analysed using PHI MultiPak software (V9.0). High-resolution scans of C 1*s*, N 1*s*, O 1*s*, Co 2*p*, Cr 2*p*, Mo 3*d*, and P 2*p* were obtained at a 23.5 eV pass in 0.05 eV steps.

## Results and Discussion

***OCP, PDP, and EIS measurements of the complex surface layer.***—To evaluate the role of the BSA protein molecule in the electrochemical response, OCP, PDP, and EIS measurements were used during protein adsorption on the complex oxide layer of the CoCrMo alloy immersed in the PBS solution. The OCP curves obtained for the solutions containing different BSA concentrations (Fig. 1a) clearly show that the OCP of the CoCrMo gradually increased, which is mainly related to the passive film growth during immersion for 1 h. Adding BSA protein to the solutions containing 0–2 g $l^{-1}$ of PBS decreased the potential from −190 mV (0 g $l^{-1}$ of BSA) to −280 mV vs Ag/AgCl (2 g $l^{-1}$ of BSA) after 1 h immersion time. As stated previously,[35,39] this result can be attributed to the cathodic inhibition of the BSA, which acted as an inhibitor and controlled the kinetics of both the metal ion release and reduction reactions, including oxygen and hydrogen reactions.

Figure 1b illustrates the PDP curves generated after the OCP measurements of the CoCrMo alloy immersed in PBS solution for 1 h with different BSA protein concentrations. The important electrochemical parameters of the PDP curves including the corrosion potential ($E_{corr}$), corrosion current density ($i_{corr}$) calculated using Tafel extrapolation, and passive current density ($i_{pass}$) are reported in Table I. As reported previously, by increasing the BSA protein concentration from 0 to 2 g $l^{-1}$, $E_{corr}$ decreased ($-195_{0\ g/l} > -250_{0.5\ g/l} > -292_{1\ g/L} > -330_{2\ g/l}$ mV vs Ag/AgCl) owing to the effect of the BSA protein on the cathodic reaction.[16,54] Moreover, a small peak appears on the anodic branch of the PDP curve obtained for the CoCrMo sample (inserted image) in the absence of the BSA protein during sweeping to the passivity region at approximately 72 mV vs Ag/AgCl. This peak has been attributed to the intense contribution of the chromium (Cr) as both $Cr_2O_3$ and $Cr(OH)_3$ to the growth and compaction of the passive layer.[36] Moreover, the BSA increased both $i_{corr}$ and $i_{pass}$ (Table I). Notably, gradually increasing the BSA protein concentration from 0.5 to 2 g $l^{-1}$ decreased $i_{pass}$, suggesting that at low concentrations, the complexing effect of the BSA molecules with the metal substrate plays a major role leading to greater dissolution or metal–protein complex detachment, while at higher BSA concentrations, more protein is absorbed on the surface, thereby providing a shielding effect.[1]

Under physiological conditions in the human body, inflammatory cells can release reactive oxygen species (ROSs), thus increasing the degradation of implant materials.[7] According to the results of previous studies conducted under simulated inflammation conditions, the electrochemical potential of the CoCrMo alloy can positively shift from −0.1 to +0.65 V owing to the Fenton reaction and the formation of hydrogen peroxide ($H_2O_2$).[25] Therefore, we polarized the CoCrMo samples for 1 h at anodic potentials +100 mV and +300 mV vs Ag/AgCl (compared to OCP as a reference) in all the tested solutions. Then, EIS was used to visualise the simultaneous influences of the passive film growth, protein adsorption on the positively charged passive film, and material degradation (i.e. resistance to charge transfer) on the CoCrMo samples (Fig. 2). The EIS spectra were fitted using the equivalent circuits (Figs. 2d and 2e) and ZView® software (Scribner Associates), and the results are listed in Table II.

For the non-polarized samples (i.e. under the OCP condition), only one time-constant was detected for a complex layer composed of a thin passive film, phosphate species, and an adsorbed protein layer[54] (Fig. 2). The equivalent electrical circuit (EEC) parameters are as follows: solution resistance ($R_s$), metal/complex layer resistance, and constant phase element ($R_{complex}$ and $CPE_{complex}$).

Although two time-constants were detected for the polarized samples, the low-frequency responses were assumed to correspond to the metal/oxide film ($R_{oxide}$ and $CPE_{oxide}$) and the high-frequency ones to the oxide film/adsorbed layer ($R_{ads}$ and $CPE_{ads}$).[55] Therefore, the adsorbed layer was composed of phosphate species, metal–-protein complexes, and a thin layer of adsorbed BSA protein.[54] The impedance of the *CPE*s was calculated using the following equation:[53]

$$Z_{CPE} = \frac{1}{Y_0(j\omega)^n}, \qquad [1]$$

where $Y_0$ is the modulus, $j$ is the imaginary unit, $\omega$ is the angular frequency, and $n$ is the CPE exponent ($-1 \leqslant n \leqslant 1$).

The impedance magnitude at 10 mHz was used to compare all the tested samples (Fig. 3). The CoCrMo samples polarized at +300 mV vs Ag/AgCl in the solutions containing different BSA protein concentrations exhibited a higher absolute impedance at 10 mHz or total resistance ($R_{Total} = R_s + R_{ads} + R_{oxide}$) than those in OCP and +100 mV vs Ag/AgCl polarized conditions ($Z_{+300\ mV} > Z_{+100\ mV} > Z_{OCP}$, (Figs. 2 and 3)). $R_{Total}$ increased with increasing applied overpotential because the increased thickness and compactness of the passive layer particularly affected the oxide.[54,56]

The CoCrMo alloy immersed the blank PBS solution exhibited higher impedance than the counterparts immersed in all the solutions containing various BSA protein concentrations under all the applied overpotential conditions (i.e. OCP, +100 mV, and +300 mV vsAg/AgCl). This is attributed to the adsorption of the phosphate species ($HPO_4^{2-}$ and $H_2PO_4^-$) on the oxide layer, which blocks the active sites and provides a more pronounced shielding effect compared to the adsorption of protein molecules and/or protein–metal complexes.[1] Likewise, metal phosphate complexes such as orthophosphate ($CrPO_4$) and metaphosphate ($Mo(PO_3)_3$) can form, which directly affect the absolute impedance.[1] The EEC elements (Table II) show that the resistances of the adsorbed layer ($R_{ads}$) and the oxide film ($R_{oxide}$) in the polarized samples both improved with increasing BSA protein concentration from 0.5 to 2 g $l^{-1}$. Therefore, when the protein concentration was increased from 0.5 to 2 g $l^{-1}$, the resistances slightly increased, which in turn directly increased the absolute impedances measured at 10 mHz (Fig. 3). This could be because when the solution contained a high BSA concentration, the BSA strongly adsorbed on the metal or oxide surfaces by electrostatic or hydrophobic (i.e. chemisorption through carboxylate/amino groups) interactions and then inhibited the electrochemical reactions.[2,39] When the solution contained a low BSA concentration, on the other hand, the BSA could compete with the phosphate

**Table I $i_{corr}$, $E_{corr}$ and $i_{pass}$ data which obtained from PDP curves in Fig. 1b.**

| BSA concentration (g.$l^{-1}$) | $i_{corr}$ (A.$cm^{-2}$) | $E_{corr}$ (mV vs Ag/AgCl) | $i_{pass}$ (A.$cm^{-2}$) |
|---|---|---|---|
| 0 | $0.7 \pm 0.3 \times 10^{-7}$ | −195 ± 15 | $1.6 \pm 0.3 \times 10^{-6}$ |
| 0.5 | $2.4 \pm 0.5 \times 10^{-7}$ | −250 ± 30 | $4.2 \pm 0.4 \times 10^{-6}$ |
| 1 | $1.9 \pm 0.4 \times 10^{-7}$ | −292 ± 20 | $3 \pm 0.2 \times 10^{-6}$ |
| 2 | $1.2 \pm 0.2 \times 10^{-7}$ | −330 ± 25 | $2.5 \pm 0.2 \times 10^{-6}$ |

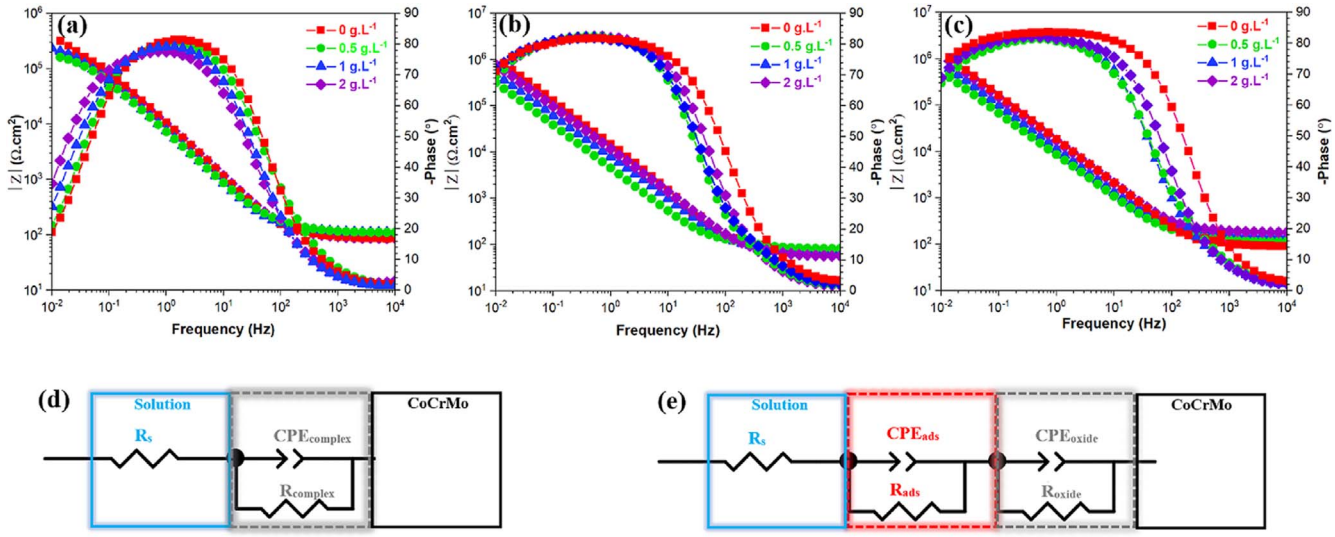


**Figure 2.** Bode phase and Bode magnitude diagrams of CoCrMo alloy in the PBS solution with the various concentrations of BSA protein at 37 °C, pH 7.4, and aerated condition, after 1 h polarization at (a) OCP, (b) +100 mV vs Ag/AgCl, (c) +300 mV vs Ag/AgCl, equivalent electrical circuits of EIS measurements into (d) one time constant (e) two-time constants.

species for surface adsorption, thereby weakening the protective effect of the adsorbed phosphate species on the passive thin film.[55]

***Protein–oxide complex surface analysis by XPS.***—XPS surface analysis was used to reveal the influence of different applied overpotentials (i.e. OCP and only +300 mV vs Ag/AgCl) on the chemical distribution and BSA protein adsorption on the complex oxide layer of the CoCrMo alloy. To interpret the synergistic effect of the applied overpotential and BSA protein adsorption on the release of metal ions, the individual high-resolution XPS spectra of the main elements are shown (Fig. 4), including Co 2*p*, Cr 2*p*, Mo 3*d*, P 2*p*, C 1*s*, N 1*s*, and O 1*s* together with the elemental distributions on the CoCrMo oxide layer surface calculated from the XPS results (Fig. 4h).

The Co spectrum presents two peaks corresponding to Co $2p_{3/2}$ and $2p_{1/2}$ at binding energies of 777.9 and 792.5 eV, respectively, alongside one peak corresponding to cobalt hydroxide ($Co(OH)_2$) at 781.5 eV.[34] Moreover, four peaks corresponding to Cr were detected in the Cr spectrum, including $Cr_2O_3$ $2p_{3/2}$ and $2p_{1/2}$ at binding energies of 576.4 ± 0.1 and 586.1 ± 0.1 eV, respectively, and $Cr^0$ $2p_{3/2}$ and $2p_{1/2}$ at binding energies of 573.5 ± 0.6 and 582.5 ± 0.6 eV, respectively.[36] The Mo spectrum exhibits three main peaks including two corresponding to metallic Mo at binding energies of 227.8 eV (Mo $3d_{5/2}$) and 231.0 eV (Mo $3d_{3/2}$) and one corresponding to $MoO_3$ at a binding energy of 232.5 eV ($3d_{5/2}$).[34,36,57] In the C spectrum, the main C peaks originated from airborne carbon or contamination. However, BSA was included in both CO–NH peptides and amino ($–NH_2$) and carboxyl (–COOH) groups.[58]

Thus, the C 1*s* peaks can be deconvoluted into three peaks at binding energies of 284.8 ± 0.2, 286.0 ± 0.1, and 287.8 ± 0.2 eV, which are related to mainly C–C and C–H bonds, peptidic residues or C–O and C–N bonds, and N–C=O bonds, respectively,[28,59] suggesting that the higher-intensity C and N peaks obtained for the surface layer of the CoCrMo immersed in the BSA solution are attributed to the BSA protein adsorption on the oxide surface. Likewise, the P spectrum (P $2p_{3/2}$) peak was distinguished between binding energies of 133.2 eV and 134.1 eV.[54] The O 1*s* spectrum exhibited two dominant peaks originating from oxide ($O^{2-}$) at 530.4 ± 0.5 eV and hydroxide or hydroxyl groups at 531.8 ± 0.3 eV arising from metal oxides and oxidised surface carbon.[34] The surface oxide layer of the CoCrMo was highly enriched with Co, Cr, and Mo oxides under the OCP and +300 mV vs Ag/AgCl conditions only for the samples immersed in the blank PBS solution (Fig. 4). However, with the addition of BSA protein

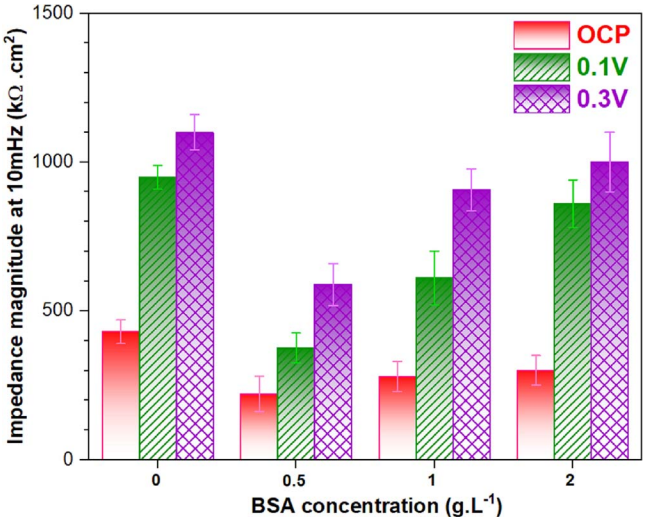


**Figure 3.** Impedance magnitude at 10 mHz $|Z_{10\ mHz}|$ for all CoCrMo specimens at different applied overpotentials and protein concentrations.

to the PBS solution, the surface oxide layer exhibited less distribution of Co, Cr, and Mo under both the OCP and +300 mV vs Ag/AgCl overpotential conditions. Likewise, the BSA protein environment significantly inhibited the formation and growth of the complex oxide layer on the CoCrMo surface, which was accompanied by a weakening O spectrum signal[54,60] (Figs. 4g and 4h). Notably, the BSA protein layer (approximately 6–8 nm thick as calculated by the AFM maps in Fig. 9) covering the oxide layer slightly affected the Co, Cr, and Mo contents in the passive film.

When BSA protein was added to the PBS solution, the P elemental distribution on the oxide layer surface of the CoCrMo alloy remarkably decreased under both the OCP and +300 mV vs Ag/AgCl conditions (Figs. 4f and 4h). Therefore, the BSA molecules inhibited and controlled the adsorption of the phosphate species on the surface of the CoCrMo complex oxide layer. These results are in accordance with those of a previous study, which showed that BSA protein remarkably slowed the ionic diffusion of the calcium and phosphate species to adsorption and then to the formation of the surface crystal.[54,61] Indeed, when the BSA concentration was increased, the nucleation and crystal growth of the calcium-

**Table II. EIS extracted parameters for CoCrMo alloy in the presence of different BSA protein concentrations and overpotential conditions in Fig. 2.**

| Condition ( $g.l^{-1}$ BSA) | $R_s$ ($\Omega.cm^2$) | $R_{ads}$ ($k\Omega.cm^2$) | $CPE_{ads}$ ($\mu\Omega^{-1}.s^n.cm^{-2}$) | $n_{ads}$ | $R_{complex/oxide}$ ($M\Omega.cm^2$) | $CPE_{complex/oxide}$ ($\mu\Omega^{-1}.s^n.cm^{-2}$) | $n_{complex/oxide}$ |
|---|---|---|---|---|---|---|---|
| OCP | | | | | | | |
| 0 | 90 ± 4 | | | | 0.41 ± 0.02 | 52 ± 2 | 0.92 ± 0.03 |
| 0.5 | 123 ± 10 | | | | 0.18 ± 0.06 | 60 ± 2 | 0.91 ± 0.02 |
| 1 | 127 ± 5 | | | | 0.24 ± 0.05 | 82 ± 2 | 0.91 ± 0.01 |
| 2 | 88 ± 6 | | | | 0.26 ± 0.05 | 108 ± 2 | 0.90 ± 0.02 |
| **+100 mV** | | | | | | | |
| 0 | 112 ± 6 | 0.45 ± 0.3 | 238 ± 40 | 0.82 ± 0.01 | 1.02 ± 0.04 | 50 ± 10 | 0.96 ± 0.02 |
| 0.5 | 96 ± 5 | 0.32 ± 0.5 | 254 ± 40 | 0.80 ± 0.02 | 0.34 ± 0.05 | 66 ± 7 | 0.94 ± 0.01 |
| 1 | 79 ± 5 | 0.32 ± 0.3 | 260 ± 50 | 0.83 ± 0.01 | 0.56 ± 0.09 | 72 ± 3 | 0.94 ± 0.01 |
| 2 | 76 ± 5 | 0.37 ± 0.4 | 270 ± 70 | 0.84 ± 0.02 | 0.94 ± 0.08 | 78 ± 2 | 0.97 ± 0.03 |
| **+300 mV** | | | | | | | |
| 0 | 123 ± 3 | 0.49 ± 0.4 | 250 ± 50 | 0.80 ± 0.01 | 1.15 ± 0.06 | 54 ± 5 | 0.92 ± 0.02 |
| 0.5 | 128 ± 5 | 0.33 ± 0.2 | 265 ± 60 | 0.81 ± 0.02 | 0.54 ± 0.05 | 71 ± 4 | 0.92 ± 0.03 |
| 1 | 145 ± 7 | 0.42 ± 0.3 | 280 ± 30 | 0.81 ± 0.01 | 0.95 ± 0.07 | 76 ± 6 | 0.94 ± 0.02 |
| 2 | 214 ± 4 | 0.40 ± 0.6 | 290 ± 50 | 0.85 ± 0.02 | 1.04 ± 0.1 | 87 ± 5 | 0.95 ± 0.01 |

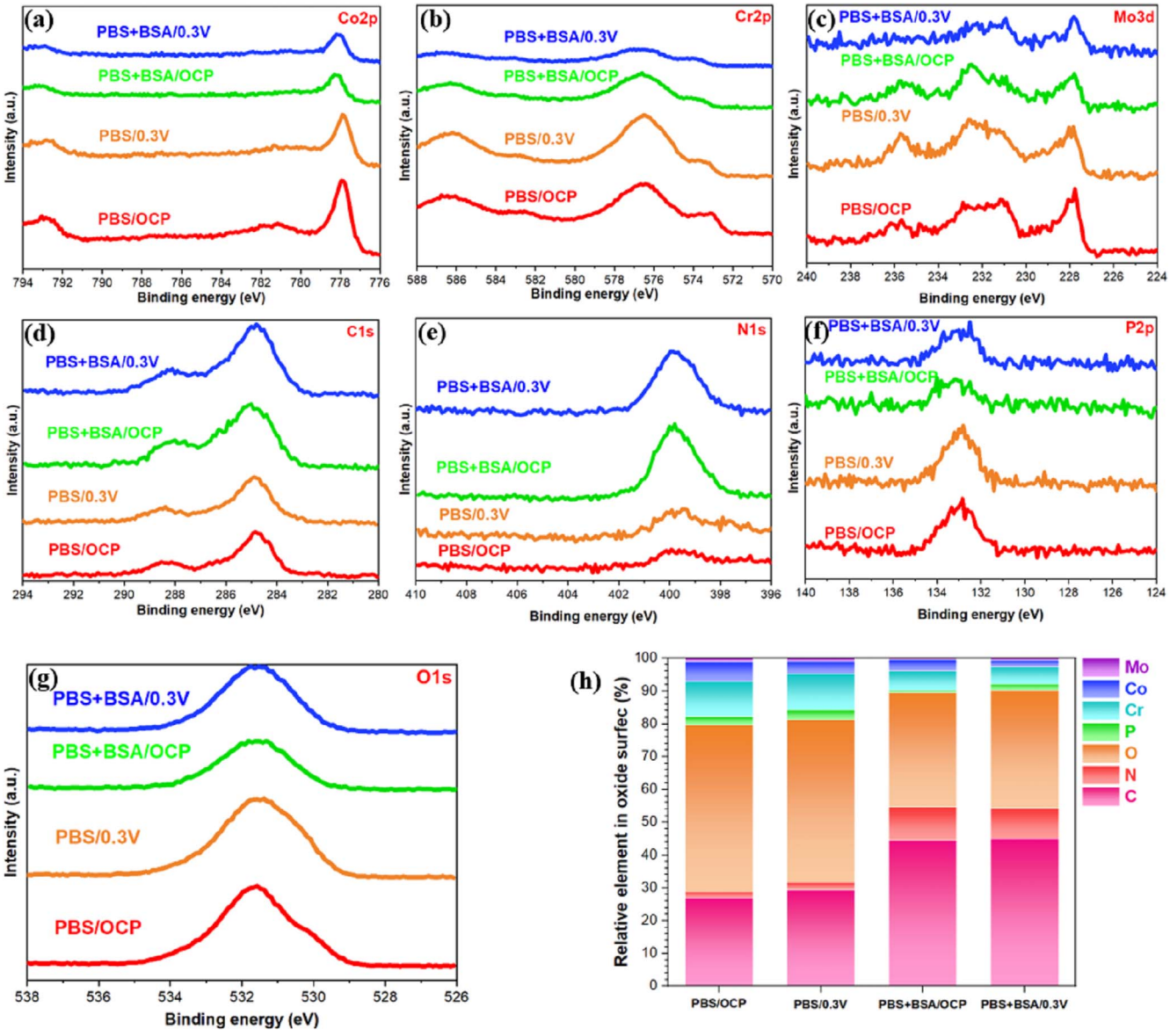


**Figure 4.** XPS spectra of (a) Co2p, (b) Cr2p, (c) Mo3d, (d) C1s, (e) N1s, (f) P2p, and (g) O 1s electron energy regions on CoCrMo alloy after exposing to PBS solution for 1 h at OCP and +300 mV vs Ag/AgCl with and without 2 $g.l^{-1}$ BSA, (h) Relative element in surface oxide obtained from XPS spectra.

phosphate species were both notably inhibited, thereby affecting the surface morphology. In the PBS environment, $HPO_4^{2-}$ and $H_2PO_4^-$ are the dominant species that can easily adsorb onto CoO, $Cr_2O_3$, and $MoO_3$ oxide surfaces to form a thin phosphate-complex film.[1] In the P spectrum, the P $2p_{3/2}$ peak at a binding energy of 133.4 eV originated from $CrPO_4$.[35] The thin phosphate-rich layer formed on the surface of the CoCrMo complex oxide immersed in the blank PBS solution offers better degradation protection compared to the PBS + BSA environment, thereby hindering the release of Co, Cr, and Mo ions or blocking the mass transport.

A precise correlation can be established between the lowest Co, Cr, and Mo concentrations and the highest C and N contents on the surface oxide layer of the CoCrMo when the samples were polarized at +300 mV vs Ag/AgCl and immersed in the PBS + BSA environment. Indeed, when a positive surface charge (+300 mV vs Ag/AgCl) was applied, the BSA molecules exhibiting a negative zeta potential[62] tended to adsorb strongly owing to electrostatic interaction with the complex oxide layer, which finally triggers higher protein adsorption (i.e. higher C and N contents). This was confirmed by FE-SEM and AFM/SKPFM surface analyses, which will be discussed in the next section. Figure 5 shows a schematic representation of the impact of the BSA protein on the metal ions released from the CoCrMo surface at different overpotentials.

***Surface potential and protein conformational arrangements.***— The CoCrMo alloy exhibiting heterogeneous oxide components during exposure to the simulated physiological environment can show different adsorption mechanisms for various ions and protein species, protein conformations, and metal-ion releases. When a positive overpotential is applied to the alloy, the aforementioned parameters can change because of new evolutions on the surface oxide layer, including chemical compositions (as determined by XPS), nanometric roughness, and WFEs exhibiting occupied and unoccupied densities of state.[63] Figure 6 presents the AFM and SKPFM maps of the CoCrMo specimens immersed in PBS + 0.5 $g\,l^{-1}$ of BSA for 1 h at different applied overpotentials including OCP, +100 mV, and +300 mV vs Ag/AgCl. In addition, the AFM and SKPFM maps of a polished or fresh CoCrMo alloy surface are reported as a reference (Fig. 7).

The AFM topography map of the sample to which the OCP was applied (Fig. 6a) clearly reflects the microstructure of the CoCrMo alloy, wherein different grains and twins are visible (without any

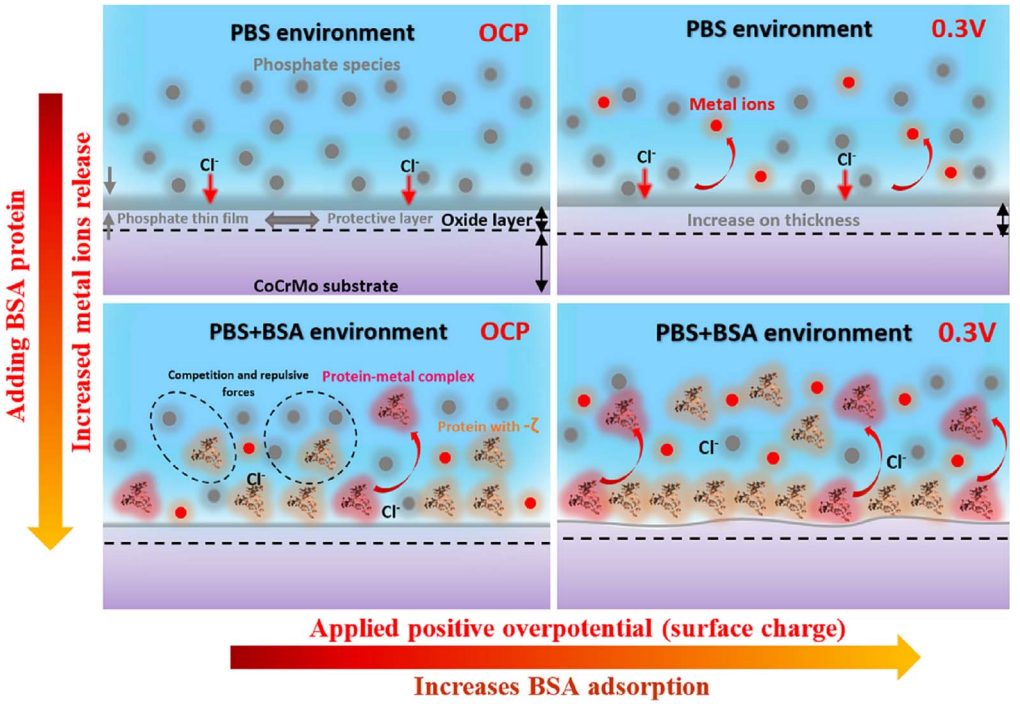


**Figure 5.** Schematic representation of the applied overpotential impact on the BSA protein adsorption and metal ion release on the surface of CoCrMo alloy.

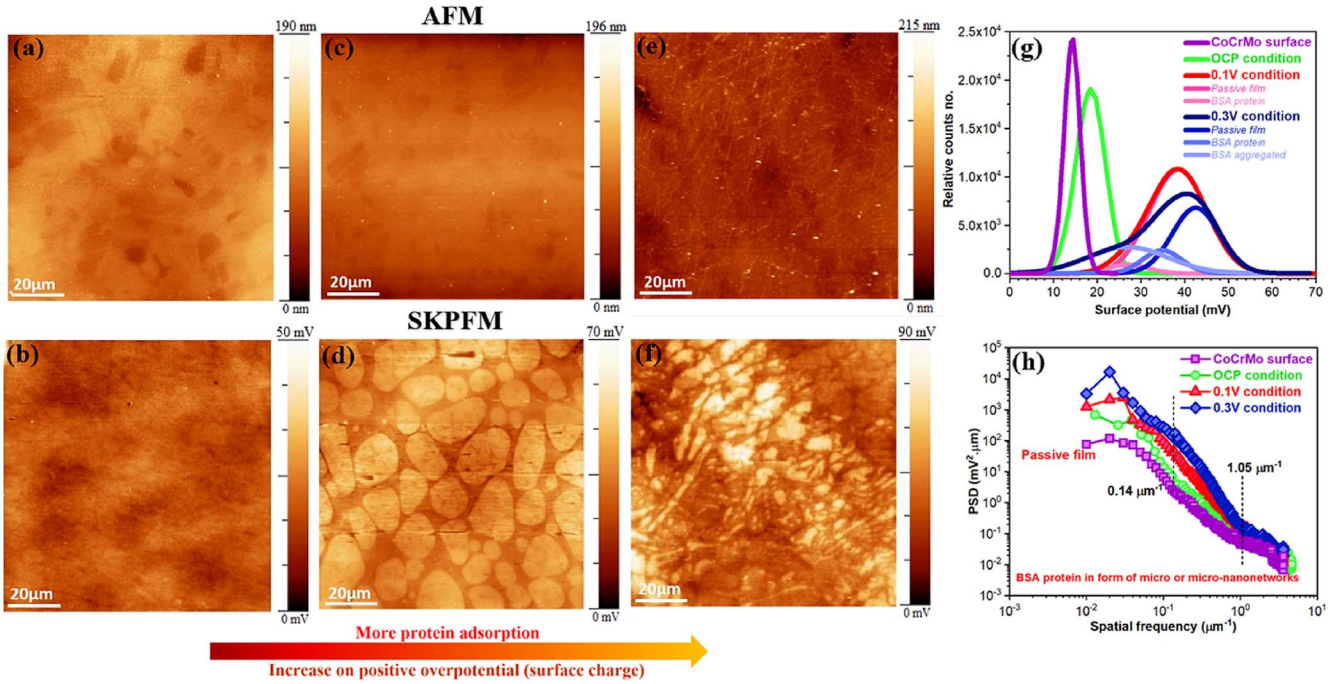


**Figure 6.** AFM (first row) and SKPFM (second row) images of CoCrMo alloy polarized for 1 h at different overpotentials (a), (b) OCP, (c), (d) +100 mV vs Ag/AgCl, (e),( f) +300 mV vsvs Ag/AgCl, in PBS + 0.5 g.l$^{-1}$ BSA protein environment, (g) The surface potential histogram and (h) PSD plots related to SKPFM maps.

evidence of protein formation). However, when positive overpotentials of +100 mV and then +300 mV vs Ag/AgCl were applied, the features of the alloy microstructure gradually disappeared and the BSA protein micro-/nano-networks gradually formed on the CoCrMo surface (Figs. 6c and 6e). Because SKPFM is very sensitive to surface evolution, the corresponding surface potential maps demonstrate a homogenously distributed surface potential under OCP conditions (Fig. 6b). In contrast, at +100 mV and +300 mV vs Ag/AgCl, BSA protein micro-/nano-networks were heterogeneously distributed in the surface-potential images (Figs. 6d and 6f). At high resolutions of 1 × 1 $\mu m^2$ and 500 × 500 $nm^2$, the CoCrMo surface to which the OCP was applied (Fig. 8) exhibited uniform adsorption of BSA protein as denatured and aggregated shapes, suggesting that the applied positive overpotential significantly affected the shape and amount of protein adsorption and, in turn, the surface potential distribution. Albumin is the strongest metal binder among human

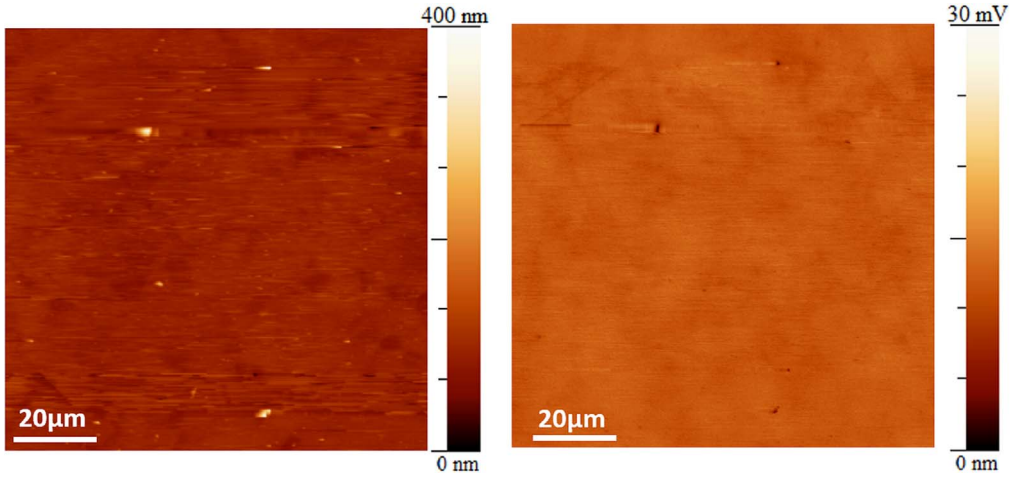


**Figure 7.** (a) AFM and (b) SKPFM images of the CoCrMo polished surface.

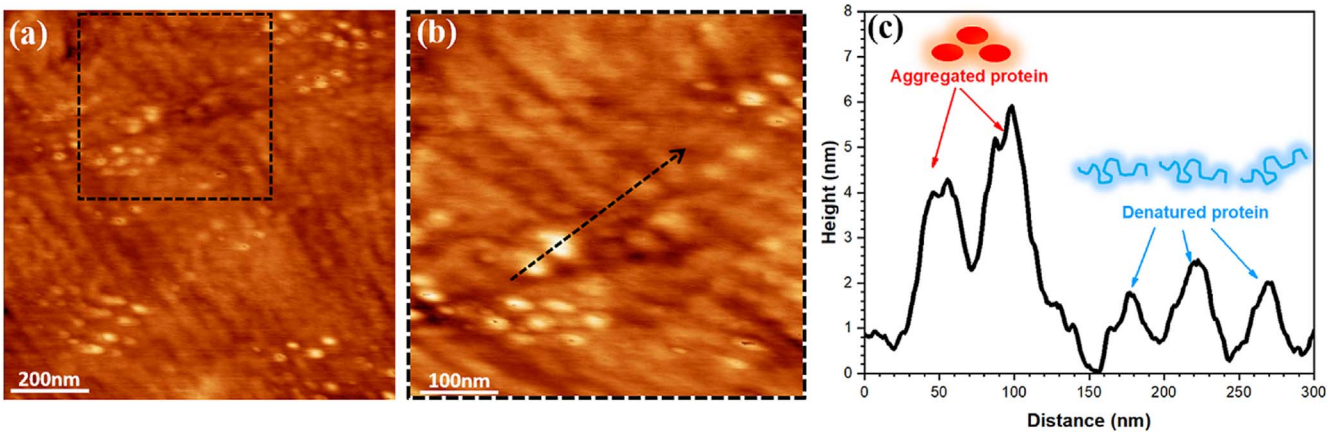


**Figure 8.** (a) Topography image of adsorbed BSA protein on CoCrMo alloy after 1 h immersion in PBS + 0.5 $g.l^{-1}$ BSA solution at OCP, 37 °C, pH 7.4, and aerated conditions, (b) Higher magnification image of marked region in (a), (c) The topography line profile in (b).

**Table III. Extracted Gaussian distribution parameters from the surface potential histograms in Figs. 6 and 9.**

| Region label | Constituents | Mean value of surface potential (mV) |
|---|---|---|
| CoCrMo alloy | Substrate | 14.3 ± 3.4 |
| **0.5 $g.l^{-1}$ BSA protein** | | |
| OCP | Substrate+BSA protein | 18.4 ± 4.7 |
| +100 mV | Substrate | 38.5 ± 10.1 |
| | BSA protein | 26.8 ± 9.6 |
| +300 mV | Substrate | 42.5 ± 10.7 |
| | BSA protein | 34.8 ± 8.7 |
| | BSA aggregated | 28.7 ± 16.2 |
| **2 $g.l^{-1}$ BSA protein** | | |
| OCP | Substrate | 37.5 ± 6.4 |
| | BSA protein | 30.7 ± 12.5 |
| +100 mV | Substrate | 53.1 ± 30.4 |
| | BSA protein | 37.3 ± 26.5 |
| +300 mV | Substrate | 56.3 ± 16.4 |
| | BSA protein | 42.1 ± 15.1 |

blood proteins and is present in high concentrations in synovial fluid.[10] BSA molecules are approximately 4 × 4 × 14-nm ellipsoids.[23]

The aggregated BSA proteins (Fig. 8c) present heights in the range 4–6 nm, while the height of the denatured proteins is approximately 3 nm. Moreover, the width (or length) of both the denatured and aggregated BSA proteins is approximately 20–40 nm, which is wider (or longer) than the aforementioned real size of the BSA molecule. However, this deviation is due to the AFM tip–-sample interaction, and the correction is approximately 10–20 nm according to a previous study.[29] The conformational or structural changes in a protein molecule from a uniform morphology to a

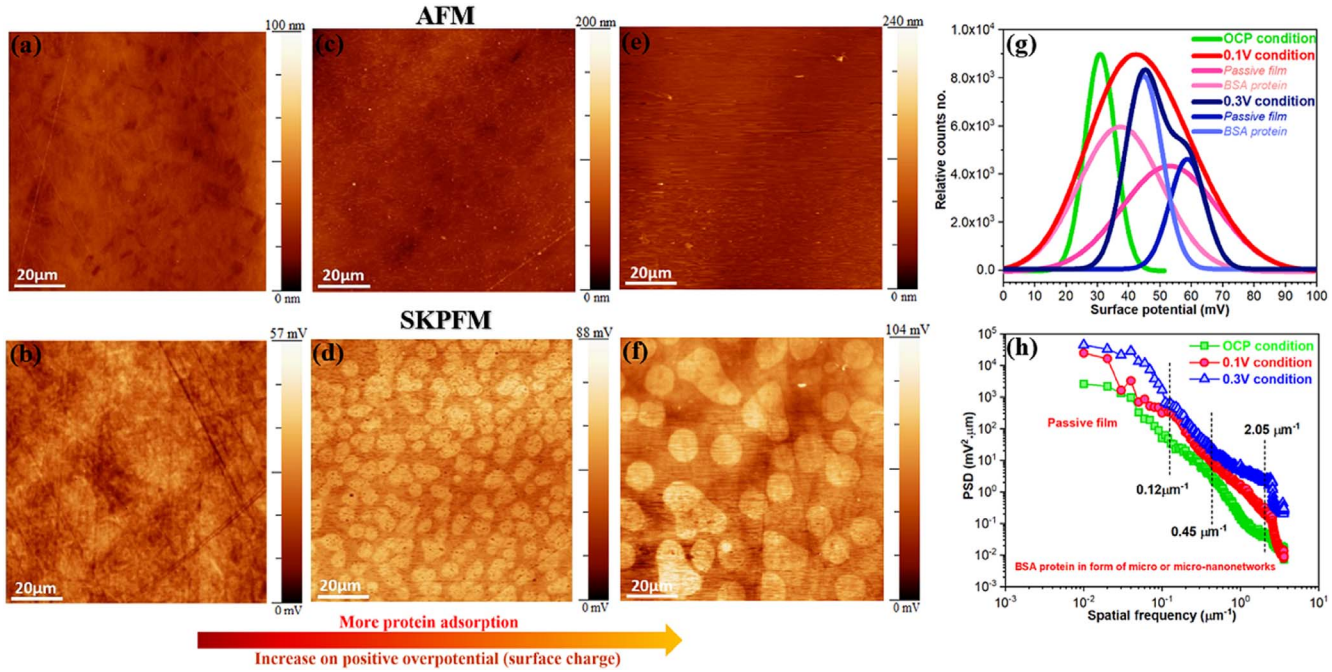


**Figure 9.** AFM (first row) and SKPFM (second row) images of CoCrMo alloy polarized for 1 h at different overpotentials (a), (b) OCP, (c), (d) +100 mV vs Ag/AgCl, (e), (f) +300 mV vs Ag/AgCl in PBS + 2 g.l$^{-1}$ BSA protein environment, (g) The surface potential histogram and (h) PSD plots related to SKPFM maps.

heterogeneous or network one are related to the surface properties of the substrate and migratory parameters.[64] These properties could synergistically affect protein adsorption mechanisms, including Langmuir isotherms and cooperative adsorption.

The surface potential image obtained at OCP (Fig. 6b), suggests that the main mechanism by which BSA protein molecules adsorb on the oxide layer of the CoCrMo alloy surface is based on the Langmuir adsorption model, wherein BSA proteins tend to fill the available unoccupied surface sites and the density of the adsorbed proteins somewhat fluctuates owing to the heterogeneity of the oxide layer. However, polarization at both +100 mV and +300 mV vs Ag/AgCl changed the BSA protein molecular adsorption mechanism into cooperative adsorption dominated by the electrostatic force because the positive surface charge could overcome the hydrophobic protein–surface interactions. According to the cooperative adsorption mechanism, BSA protein molecules preferentially adsorb in the vicinity of other pre-absorbed proteins, and then self-migration and lateral movements lead to a special morphology distribution.[22] This network or cluster morphology has been reported in a previous study in which FE-SEM was used to examine the morphology and AFM-peak force deformation maps were used for a CoCrMo alloy cathodically polarized at −0.9 V vs a saturated calomel electrode (SCE) in PBS + 15 g l$^{-1}$ BSA media at 37 °C.[65]

The BSA protein regions exhibited lower surface potentials with respect to the substate (Figs. 6b, 6d and 6f). Notably, the electrostatic surface potentials of biological molecules strongly depends on the isoelectric point (IEP) and the surrounding surface charge of the substrate.[48] Moreover, the pH indicates that the protein surface charge is minimised, as defined by IEP.[66] Based on theoretical calculations and experimental measurements, the IEP of the BSA protein is between 4.7 and 5.4%mechanisms of photo-assisted charge[12,66] At pH 7.4, the BSA protein presents a negative zeta potential, and the positive surface charge on the oxide layer during anodic polarization leads to strong BSA protein adsorption by electrostatic attraction. Therefore, +300 mV vs Ag/AgCl polarization induces high BSA protein adsorption and more heterogeneity of both the surface potential and conformational arrangement (Figs. 6e and 6f). In fact, more protein unfolding or denaturation was observed at polarization under the +300 mV vs Ag/AgCl condition than those in OCP and +100 mV vs Ag/AgCl conditions.

The histograms of the surface potentials conducted under different conditions (Fig. 6g) show one uniform peak for both polished CoCrMo and the OCP, a bi-modal peak distribution (i.e. substrate and BSA protein) when the CoCrMo was polarized at +100 mV vs Ag/AgCl, and a tri-modal peak distribution (i.e. substrate, BSA protein, and aggregated BSA protein) when the CoCrMo was polarized at +300 mV vs Ag/AgCl. The deconvoluted histograms and extracted Gaussian distribution parameters are presented in Table III. Clearly, when the experimental conditions were changed from the polished or fresh CoCrMo alloy to the OCP and finally to polarization at +300 mV vs Ag/AgCl, the total surface potential increased, as all the peaks shifted toward higher values due to the synergistic effect of the oxide film growth and the BSA protein adsorption (Table III and Fig. 6g). Moreover, from the SKPFM maps, changes in the morphology of the adsorbed protein clusters could be observed. When the specimens were polarized at +100 mV vs Ag/AgCl, the protein formed large clusters in the range 2–15 $\mu$m (Fig. 6d), while when polarized at +300 mV vs Ag/AgCl, the protein exhibited a fibrillar morphology consisting of narrower clusters of approximately 200 nm to 4 $\mu$m (Fig. 6f). From the PSD profiles of the surface potential images (Fig. 6h), all the surface features of the CoCrMo (i.e. substrate and BSA protein) polarized at +300 mV vs Ag/AgCl exhibited higher PSD magnitude (mV$^2$.$\mu$m) than the CoCrMo under the other conditions over the entire range of spatial frequencies. In addition, the higher spatial frequencies in the PSD profiles (Fig. 6h) indicate that the BSA protein regions exhibited the lowest surface potential. Moreover, the lower spatial frequencies exhibiting the highest PSD magnitude were attributed to the substrate (i.e. oxide layer) exhibiting the highest surface potential, which were higher for the specimens polarized at +300 mV vs Ag/AgCl than OCP and +100 mV vs Ag/AgCl conditions.[46]

When the BSA protein concentration was increased from 0.5 to 2 g l$^{-1}$ in the PBS solution, more of the CoCrMo surface was covered with BSA protein exhibiting fibrillar morphology for the sample at the OCP and exhibiting micro-/nano-networks for the samples polarized at +100 mV and +300 mV vs Ag/AgCl (Fig. 9). As mentioned above, only the surface potential map at OCP + 0.5 g l$^{-1}$ (Fig. 6b) presented the uniform surface potential distribution, without any evidence of BSA protein, whereas in 2 g l$^{-1}$ BSA,

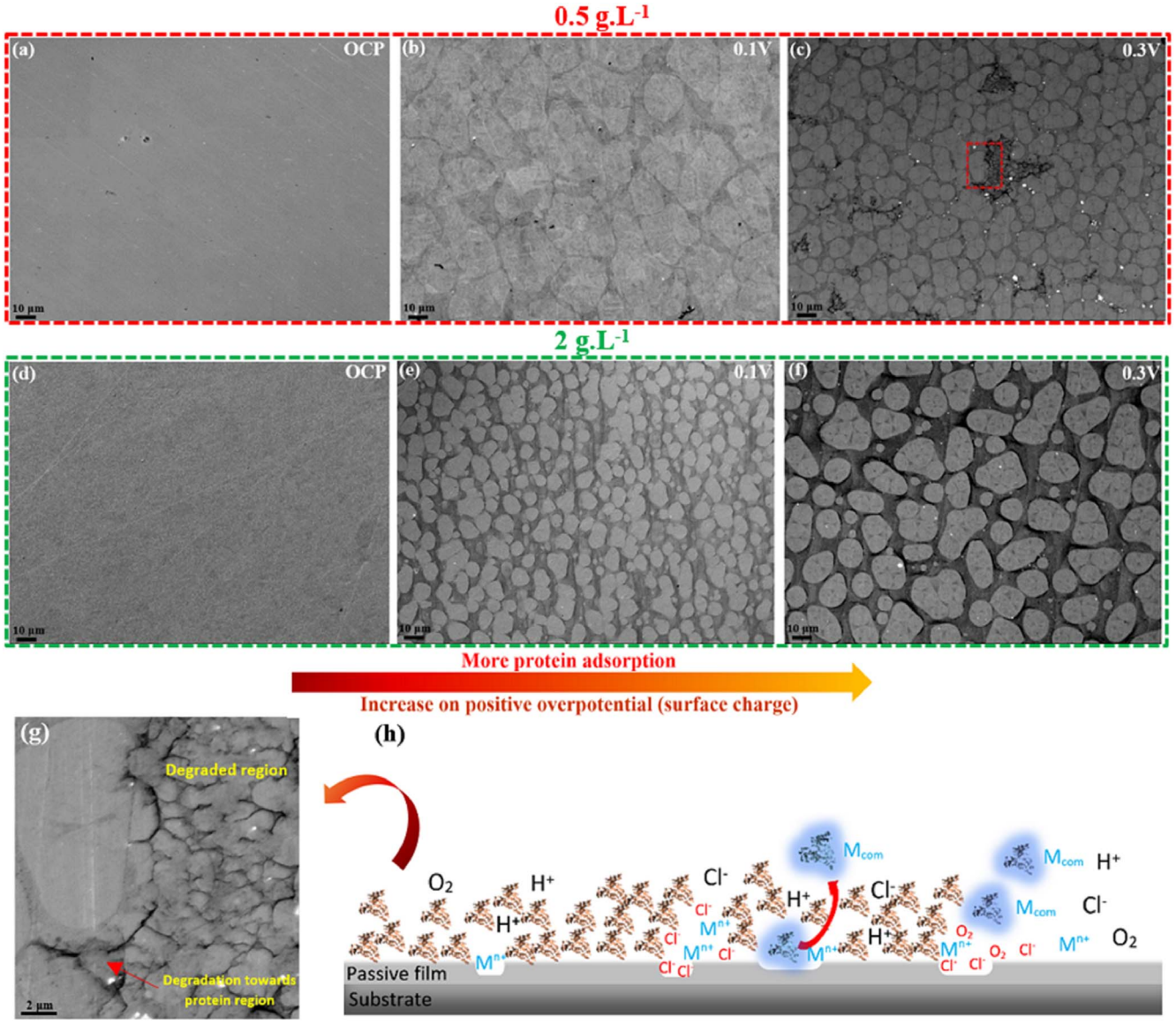


**Figure 10.** SEM images of CoCrMo alloy after 1 h polarization at OCP, +100 mV, and +300 mV vs Ag/AgCl at 37 °C, pH 7.4, and aerated conditions in PBS plus (a)–(c) 0.5 g.l$^{-1}$ and (d)–(f) 2 g.l$^{-1}$ BSA concentration; (g) SEM image of the marked region in (c), (h) a schematic representation for degradation process on CoCrMo alloy in the presence of BSA protein with different mechanisms after passing time (short or long-term).

a fibrillar morphology of BSA protein is detectable at OCP conditions (Fig. 9b).

Notably, the large domain or micro-networks of the BSA protein were in the range 5–20 $\mu$m for the sample polarized at +300 mV vs Ag/AgCl. According to the histogram of the surface potential maps (Fig. 9g) and the corresponding data (Table III), adding 2 g l$^{-1}$ of BSA protein to the PBS solution significantly increased the total surface potential of the surface features, including the protein regions and the substrate, compared to adding only 0.5 g l$^{-1}$ of BSA protein to the PBS solution under all the applied overpotential conditions. The PSD curves of the CoCrMo samples (Fig. 9h) revealed different slopes (2.05, 0.45, and 0.12 $\mu$m$^{-1}$) under all the overpotential conditions and a heterogeneously distributed PSD magnitude over all the spatial frequencies, which is consistent with the higher standard deviation as observed in histogram analyses (Table III).

***Degradation phenomena on the complex oxide layer.***—As reported in the previous sections, the BSA protein concentration and the applied overpotentials both considerably controlled the type and amount of BSA adsorption, its morphology, the elemental distribution on the CoCrMo oxide layer, and the metal ions released. To visualise the synergistic effect of both the BSA protein concentration and the applied overpotential on the degradation of the CoCrMo, the alloy surface was observed using FE-SEM (Fig. 10). Based on the BSA protein morphology distribution, a correlation can be established between the surface potential maps (Figs. 6 and 9) and the FE-SEM images. However, different regions exhibiting intensely localized corrosion attack are clearly visible on the samples immersed in 0.5 g l$^{-1}$ of BSA and polarized at +300 mV vs Ag/AgCl (darker regions in Fig. 10c) extended over the whole surface of the observed specimen. These attacks are mainly localized at the protein/substrate interface (Fig. 10g), which is consistent with our prior work[54]

Clearly, the CoCrMo surface layer was intensively degraded (i.e. the passive film breakdown), especially near the BSA protein region. Nevertheless, these types of corrosion attacks were not observed for the sample immersed in the 2 g l$^{-1}$ BSA solution and polarized at +300 mV vs Ag/AgCl. This could be because higher protein concentrations can strongly hinder the metal ion releasing process and the

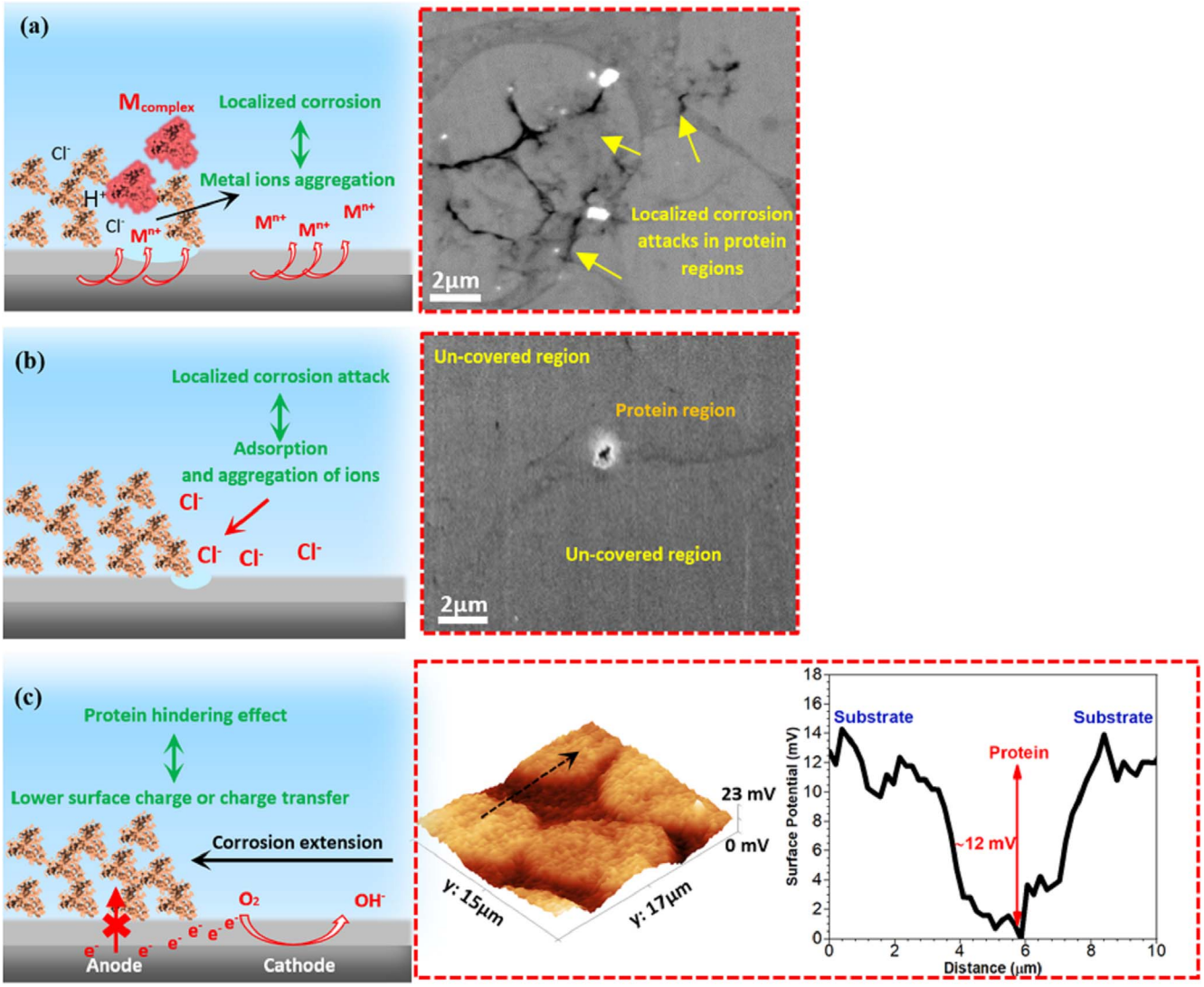


**Figure 11.** A schematic plus real evidence representation of CoCrMo alloy degradation in the presence of BSA protein with different mechanisms including (a) crevice corrosion due to aggregation of released metal ions in covered protein region which cause to more acidify and metal-protein complex formation, (b) Pitting corrosion due to adsorption and aggregation of counterions at the interface between covered protein region and un-covered protein regions and (c) Formation of anodic and cathodic zones only in OCP condition due to difference on local electrical surface potential or surface charge between protein covered region (low surface charge transfer) and protein un-covered region.

initiation of localized corrosion attacks, as stated in the electrochemical measurements section. The different degradation mechanisms of metallic implants during interaction with various protein molecules such as human serum albumin (HSA), fibronectin, and BSA proteins can be categorised as follows: (1) shielding or inhibition of cathodic reactions, (2) attraction of counterions, (3) complexation with various oxide constituents, and (4) the Vroman effect (Fig. 10h).

The BSA protein initially decreases the release of metal ions owing to the shielding effect by inhibiting the cathodic reactions on the passive film. However, depending on the time frame (from milliseconds to years), the BSA can trigger an increase in the release of metal ions.[2,10] However, the interface between the BSA-covered and un-covered regions attracts counterions (such as $Cl^-$). Thus, in such regions, counterions can penetrate the adsorbed protein layer, reach the passive film region, and eventually promote localized corrosion (Fig. 10c). The metal–protein conjugates formed owing to the complexation of the BSA with metal or metal–oxide species on passive film surfaces is another reason that metallic implants degrade.[14,67] Moreover, the Vroman effect intensifies the corrosion of metallic implants in protein environments owing to the detachment of metal–protein bonds under the control of the adsorbed protein exchange.

It is important to clarify the physiological environment and surface chemistry (as previously discussed), which directly influence the degradation intensity of implanted material and its corrosion/biodegradation mechanism time. The BSA molecules act as a barrier to control the kinetics of the mass diffusion at solution/protein/oxide layer interfaces (Fig. 11a). Therefore, phosphate or other species in the solution especially metal ions released from the oxide layer tend to accumulate under the BSA protein layer, while the un-covered region (i.e. substrate) has easy access to the metal ions released into the physiological media. This phenomenon provides an important condition for reducing the pH around the protein-covered/ un-covered substrate interface region because of the acidifying mechanism induced by the metal ions and eventually leading to crevice corrosion attack.[54,68] Another possible degradation mechanism is that counterions tend to adsorb and then precipitate in the adsorbed protein layer/exposed interface region (Fig. 11b). According to the counterion condensation theory established in biophysical models, solubilised organic species, such as DNA and/or proteins, are

surrounded by a shell of counterions for charge compensation.[50] Likewise, it has been reported that most counterions significantly influence the electrical potential surfaces of solubilised proteins and bind at defined points around protein surfaces.[69] A previous study utilising AFM/SKPFM found that a single DNA molecule adsorbed on a silicon substrate was surrounded by a salt buffer precipitate that exhibited a higher electrostatic surface potential than the DNA molecule.[50] Therefore, such interfaces where counterions (especially $Cl^-$) are highly likely to adsorb are susceptible to corrosion initiation. As stated in the SKPFM investigation (Section 3.3), the protein-enriched regions exhibited a lower electrical surface potential distribution than the un-covered regions, which means that weak electrostatic or Coulombic interactions can be established between the protein layer and the AFM tip.[66] This insight explains why the adsorbed protein region tends to lower the charge transfer from the oxide layer under the top protein layer.[70,71] In our previous study on the interaction between the BSA protein and the Ti6Al4V alloy,[54] localized corrosion attacks were visualised using SEM at the protein/Ti6Al4V interface owing to crevice corrosion and the difference between the surface potentials of the protein and substrate regions. Consequently, two regions could be formed only when the samples were at the OCP or when an overpotential was not applied, including in the cathodic zone or the nobler region (which had better access to free electrons for reduction reactions) and in the anodic zone or the active region which had less access to free electrons owing to the hindering effect of the BSA protein layer (Fig. 11c).

## Conclusions

In this study, the influence of both the BSA protein concentration and the applied overpotential on the protein adsorption mechanism, distribution/morphology, and surface potential of CoCrMo alloys was elucidated using AFM, SKPFM, XPS, FE-SEM, and electrochemical measurements.

The CoCrMo alloy exhibited the highest corrosion resistance in the blank PBS solution and improved resistance against metal ions released in the high concentration ($2\ g\ l^{-1}$) BSA protein solution compared to the low concentration ($0.5\ g\ l^{-1}$) one. The XPS analysis of the CoCrMo specimens immersed in the PBS + BSA solution and different overpotential conditions (OCP and +300 mV vs Ag/AgCl ) indicated that the intensity of the C and N peaks increased owing to BSA protein adsorption and that the Co, Cr, Mo, and O contents decreased within the passive film. FE-SEM and SKPFM images showed that when the overpotential condition on the CoCrMo surface was changed from the OCP to +100 mV and finally to +300 mV vs Ag/AgCl for 1 h, the morphology of the adsorbed BSA protein changed from a uniform protein layer to large heterogeneously distributed micro-/nano-networks. Moreover, when the surface overpotential and the protein concentration were simultaneously increased from the OCP to +300 mV vs Ag/AgCl and from 0.5 to $2\ g\ l^{-1}$, respectively, more protein covered the CoCrMo surface owing to electrostatic interaction. The SKPFM images showed a lower surface potential distribution in the BSA protein-covered regions. The histogram and PSD analyses of the surface potential maps showed that increasing the BSA protein concentration from 0.5 to $2\ g\ l^{-1}$ increased the total surface potential distribution on the CoCrMo surface. Finally, FE-SEM micrographs indicated the initiation of localized corrosion attacks at the BSA protein/substrate interface owing to the adsorption of counterions and the difference between the electrical surface potentials.

## Acknowledgments

This project has received funding from the European Union's Horizon 2020 research and innovation program under the Marie Sklodowska-Curie grant agreements No 764977.

## ORCID

Ehsan Rahimi https://orcid.org/0000-0002-7128-8940
Herman Terryn https://orcid.org/0000-0003-2639-5496
Maria Lekka https://orcid.org/0000-0001-6811-3843

## References

1. I. Milošev, *Biomedical Applications* (Springer, Berlin) p. 1 (2012).
2. M. Talha, Y. Ma, P. Kumar, Y. Lin, and A. Singh, *Colloids Surf., B*, **176**, 494 (2019).
3. M. Metikoš-Huković, Z. Pilić, R. Babić, and D. Omanović, *Acta Biomater.*, **2**, 693 (2006).
4. C. V. Vidal and A. I. Muñoz, *Corros. Sci.*, **50**, 1954 (2008).
5. L. N. Wang, A. Shinbine, and J. L. Luo, *Surf. Interface Anal.*, **45**, 1323 (2013).
6. F. Yu, O. Addison, and A. J. Davenport, *Acta Biomater.*, **26**, 355 (2015).
7. W. Xu, F. Yu, L. Yang, B. Zhang, B. Hou, and Y. Li, *Mater. Sci. Eng. C*, **92**, 11 (2018).
8. C. F. Wertz and M. M. Santore, *Langmuir*, **17**, 3006 (2001).
9. A. Ouerd, C. Alemany-Dumont, B. Normand, and S. Szunerits, *Electrochim. Acta*, **53**, 4461 (2008).
10. Y. S. Hedberg, *npj Materials Degradation*, **2**, 26 (2018).
11. N. B. Guerra, C. González-García, V. Llopis, J. C. Rodríguez-Hernández, D. Moratal, P. Rico, and M. Salmerón-Sánchez, *Soft Matter*, **6**, 4748 (2010).
12. Y. Yan, H. Yang, Y. Su, and L. Qiao, *Sci. Rep.*, **5**, 18403 (2015).
13. J. N. Meyer, M. T. Mathew, M. A. Wimmer, and R. J. LeSuer, *Anal. Chem.*, **85**, 7159 (2013).
14. A. I. Muñoz and S. Mischler, *J. Electrochem. Soc.*, **154**, C562 (2007).
15. K. Yamanaka, M. Mori, I. Kartika, M. S. Anwar, K. Kuramoto, S. Sato, and A. Chiba, *Corros. Sci.*, **148**, 178 (2019).
16. C. V. Vidal and A. I. Muñoz, *Electrochim. Acta*, **56**, 8239 (2011).
17. A. Hodgson, S. Kurz, S. Virtanen, V. Fervel, C.-O. Olsson, and S. Mischler, *Electrochim. Acta*, **49**, 2167 (2004).
18. S. J. McClellan and E. I. Franses, *Colloids Surf., A*, **260**, 265 (2005).
19. E. Bulard, M.-P. Fontaine-Aupart, H. Dubost, W. Zheng, M.-N. L. Bellon-Fontaine, J.-M. Herry, and B. Bourguignon, *Langmuir*, **28**, 17001 (2012).
20. F. A. Denis, P. Hanarp, D. S. Sutherland, J. Gold, C. Mustin, P. G. Rouxhet, and Y. F. Dufrêne, *Langmuir*, **18**, 819 (2002).
21. A. Sethuraman, M. Han, R. S. Kane, and G. Belfort, *Langmuir*, **20**, 7779 (2004).
22. H. Min et al., *Langmuir*, **33**, 7215 (2017).
23. B. Jachimska, K. Tokarczyk, M. Łapczyńska, A. Puciul-Malinowska, and S. Zapotoczny, *Colloids Surf., A*, **489**, 163 (2016).
24. P. Roach, D. Farrar, and C. C. Perry, *JACS*, **127**, 8168 (2005).
25. Y. Liu and J. L. Gilbert, *Electrochim. Acta*, **262**, 252 (2018).
26. E. Bettini, T. Eriksson, M. Boström, C. Leygraf, and J. Pan, *Electrochim. Acta*, **56**, 9413 (2011).
27. E. Bettini, C. Leygraf, and J. Pan, *Int. J. Electrochem. Sci.*, **8**, 11791 (2013).
28. Y. S. Hedberg, I. Dobryden, H. Chaudhary, Z. Wei, P. M. Claesson, and C. Lendel, *Colloids Surf., B*, **173**, 751 (2019).
29. I. Ron, L. Sepunaru, S. Itzhakov, T. Belenkova, N. Friedman, I. Pecht, M. Sheves, and D. Cahen, *JACS*, **132**, 4131 (2010).
30. C. Halliwell, J. Davies, J. Gallop, and P. Josephs-Franks, *Bioelectrochemistry*, **63**, 225 (2004).
31. S. A. Campbell, J. R. Smith, H. Jungblut, and H. J. Lewerenz, *J. Electroanal. Chem.*, **599**, 313 (2007).
32. Z. Wang, Y. Yan, Y. Su, and L. Qiao, *Appl. Surf. Sci.*, **406**, 319 (2017).
33. L. Chang, Z. Zhifeng, and L. Kwok-Yan, *Electrochim. Acta*, **241**, 331 (2017).
34. T. Hanawa, S. Hiromoto, and K. Asami, *Appl. Surf. Sci.*, **183**, 68 (2001).
35. I. Milošev, *Electrochim. Acta*, **78**, 259 (2012).
36. I. Milošev and H.-H. Strehblow, *Electrochim. Acta*, **48**, 2767 (2003).
37. X. Quan, J. Liu, and J. Zhou, *Current Opinion in Colloid & Interface Science*, **41**, 74 (2019).
38. G. Dalkas and S. R. Euston, *Current Opinion in Colloid & Interface Science*, **41**, 1 (2019).
39. S. Karimi, T. Nickchi, and A. Alfantazi, *Corros. Sci.*, **53**, 3262 (2011).
40. L. Kelvin, *The London, Edinburgh, and Dublin Philosophical Magazine and Journal of Science*, **46**, 82 (1898).
41. M. Nonnenmacher, M. o'Boyle, and H. K. Wickramasinghe, *Appl. Phys. Lett.*, **58**, 2921 (1991).
42. W. A. Zisman, *Rev. Sci. Instrum.*, **3**, 367 (1932).
43. M. Rohwerder and F. Turcu, *Electrochim. Acta*, **53**, 290 (2007).
44. V. Guillaumin, P. Schmutz, and G. Frankel, *J. Electrochem. Soc.*, **148**, B163 (2001).
45. E. Rahimi, A. Rafsanjani-Abbasi, A. Imani, and A. Davoodi, *Mater. Chem. Phys.*, **212**, 403 (2018).
46. Z. Esfahani, E. Rahimi, M. Sarvghad, A. Rafsanjani-Abbasi, and A. Davoodi, *J. Alloys Compd.*, **744**, 174 (2018).
47. A. K. Sinensky and A. M. Belcher, *Nat. Nanotechnol.*, **2**, 653 (2007).
48. M. Salerno and S. Dante, *Materials*, **11**, 951 (2018).
49. B. Moores, F. Hane, L. Eng, and Z. Leonenko, *Ultramicroscopy*, **110**, 708 (2010).
50. C. Leung, H. Kinns, B. W. Hoogenboom, S. Howorka, and P. Mesquida, *Nano Lett.*, **9**, 2769 (2009).
51. A. F-06, *Standard test Method for Conducting Cyclic Potentiodynamic Polarization Measurements to Determine the Corrosion Susceptibility of Small Implant Devices* (ASTM International, West Conshohocken, PA) (2001).
52. R. Ovarfort, *Corros. Sci.*, **28**, 135 (1988).
53. E. Rahimi, A. Rafsanjani-Abbasi, A. Kiani-Rashid, H. Jafari, and A. Davoodi, *Colloids Surf., A*, **547**, 81 (2018).

54. E. Rahimi, R. Offoiach, K. Baert, H. Terryn, M. Lekka, and L. Fedrizzi, *Materialia*, **15**, 100988 (2021).
55. C. V. Vidal and A. I. Muñoz, *Electrochim. Acta*, **55**, 8445 (2010).
56. C. V. Vidal and A. I. Muñoz, *Electrochim. Acta*, **54**, 1798 (2009).
57. S. Karimi, T. Nickchi, and A. M. Alfantazi, *Appl. Surf. Sci.*, **258**, 6087 (2012).
58. S. Karimi and A. M. Alfantazi, *Mater. Sci. Eng. C*, **40**, 435 (2014).
59. B. Wu, C. Mu, G. Zhang, and W. Lin, *Langmuir*, **25**, 11905 (2009).
60. M. A. Wimmer, A. Fischer, R. Büscher, R. Pourzal, C. Sprecher, R. Hauert, and J. J. Jacobs, *Journal of Orthopaedic Research*, **28**, 436 (2010).
61. C. Combes and C. Rey, *Biomaterials*, **23**, 2817 (2002).
62. T. Guckeisen, S. Hosseinpour, and W. Peukert, *Langmuir*, **35**, 5004 (2019).
63. A. E. Nel, L. Mädler, D. Velegol, T. Xia, E. M. Hoek, P. Somasundaran, F. Klaessig, V. Castranova, and M. Thompson, *Nat. Mater.*, **8**, 543 (2009).
64. E. Grigoriou, M. Cantini, M. Dalby, A. Petersen, and M. Salmeron-Sanchez, *Biomater. Sci.*, **5**, 1326 (2017).
65. R. Namus, J. Nutter, J. Qi, and W. M. Rainforth, *Appl. Surf. Sci.*, **499**, 143908 (2020).
66. E. Rahimi, R. Offoiach, S. Hosseinpour, A. Davoodi, K. Baert, A. Lutz, H. Terryn, M. Lekka, and L. Fedrizzi, *Appl. Surf. Sci.*, **563**, 150364 (2021).
67. E. Rahimi, R. Offoiach, S. Deng, X. Chen, S. Pané, L. Fedrizzi, and M. Lekka, *Applied Materials Today*, **24**, 101135 (2021).
68. S. Hiromoto and T. Hanawa, *Electrochem. Solid-State Lett.*, **7**, B9 (2004).
69. M. Cianci, J. Negroni, J. R. Helliwell, and P. J. Halling, *RSC Adv.*, **4**, 36771 (2014).
70. I. Ron, I. Pecht, M. Sheves, and D. Cahen, *Acc. Chem. Res.*, **43**, 945 (2010).
71. A. Liscio, V. Palermo, and P. Samorì, *Acc. Chem. Res.*, **43**, 541 (2010).